

Polymer electrolyte fuel cell performance degradation at different synchrotron beam intensities

Jens Eller and Felix N. Büchi*

Received 31 May 2013

Accepted 10 September 2013

Electrochemistry Laboratory, Paul Scherrer Institut, Villigen PSI, Switzerland.

*E-mail: felix.buechi@psi.ch

The degradation of cell performance of polymer electrolyte fuel cells under monochromatic X-ray irradiation at 13.5 keV was studied in galvanostatic and potentiostatic operation modes in a through-plane imaging direction over a range of two orders of magnitude beam intensity at the TOMCAT beamline of the Swiss Light Source. The performance degradation was found to be a function of X-ray dose and independent of beam intensity, whereas the degradation rate correlates with beam intensity. The cell performance was more sensitive to X-ray irradiation at higher temperature and gas feed humidity. High-frequency resistance measurements and the analysis of product water allow conclusions to be drawn on the dominating degradation processes, namely change of hydrophobicity of the electrode and sulfate contamination of the electrocatalyst.

© 2014 International Union of Crystallography

Keywords: polymer electrolyte fuel cell (PEFC); *in situ* X-ray imaging; radiation damage.

1. Introduction

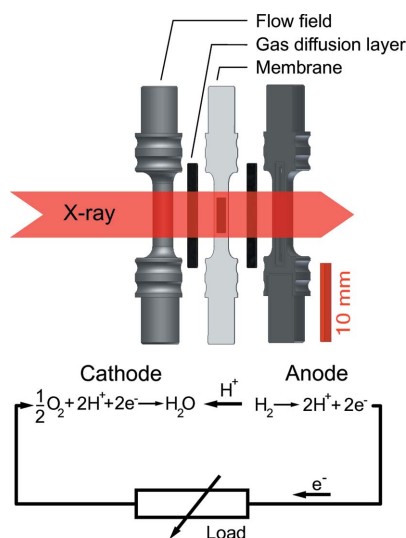
Hydrogen-fueled polymer electrolyte fuel cells (PEFCs) are an environmentally attractive option for local emission free electromobility as the only reaction product is water. The half-cell reactions of the electrochemical reaction in a PEFC are shown in Fig. 1. The efficient removal of the product water is one of the major challenges of PEFC operation, as liquid water tends to block the transport paths of hydrogen and oxygen towards the catalyst layer. The situation is complicated

by the fact that the ionic conduction of the polymer electrolyte membrane, and thus cell performance, requires a high water content of the membrane.

Synchrotron-based X-ray imaging has become a frequently used tool to visualize liquid water in PEFCs, both in radiography (Mukaide *et al.*, 2008; Hartnig *et al.*, 2009; Lee *et al.*, 2013; Alink *et al.*, 2013) and tomography (Schneider *et al.*, 2010; Eller *et al.*, 2011*a,b*; Krüger *et al.*, 2011) studies.

Opposite to that, X-ray-induced performance loss of PEFCs has been reported by only a few groups (Schneider *et al.*, 2010; Eller *et al.*, 2011*a,b*, 2014; Roth *et al.*, 2012) using beamlines at the European Synchrotron Radiation Facility (ESRF, Grenoble, France) or the Swiss Light Source (SLS, Villigen, Switzerland) and cells whose electrochemically active area fits completely into the beam. The monochromatic photon flux density used by Eller *et al.* (2011*a,b*) and Roth *et al.* (2012) at the TOMCAT beamline of the SLS and Schneider *et al.* (2010) at the ID19 beamline of the ESRF were between 6×10^{11} photons $s^{-1} mm^{-2}$ (Eller *et al.*, 2011*a*) and 10^{13} photons $s^{-1} mm^{-2}$ (Weitkamp *et al.*, 2010), respectively. The photon flux density of other beamlines used for PEFC imaging is typically lower, *i.e.* 3.5×10^{10} photons $s^{-1} mm^{-2}$ at 15 keV at BAMline (Görner *et al.*, 2001) at Helmholtz Center Berlin (Germany) used by Krüger *et al.* (2011) and Hartnig *et al.* (2009), or about 3×10^9 photons $s^{-1} mm^{-2}$ at 30 keV and 100 mA ring current at BL19B2 at SPring-8 (Harima Institute, Mikazuki, Hyogo, Japan) (Goto *et al.*, 2001) used by Mukaide *et al.* (2008).

This work intends to clarify whether the X-ray-induced PEFC performance degradation during X-ray imaging experiments depends on the X-ray dose or on the beam intensity.

**Figure 1**

Components and irradiation scheme of the X-ray tomographic microscopy cell as well as PEFC half-cell reactions. The entire catalyst layer domain (black rectangular area on membrane) is irradiated by the X-ray beam. Sub-gaskets and cell bearing are not shown.

2. Experimental

For the irradiation experiments, single channel cells designed for X-ray tomographic microscopy (XTM) investigations (Eller *et al.*, 2011a) were used (see Fig. 1). The irradiated domain of the cell consists of a catalyst-coated membrane (CCM), carbon-fiber paper gas diffusion layers (GDLs), polymer foil gaskets, carbon composite flow fields and a polyimide cell bearing. The CCM from Umicore uses a 50 μm -thick perfluorated sulfonic acid Nafion 112 membrane with a carbon support-based catalyst with the anode (cathode) Pt loading of 0.2 mg cm^{-2} (0.4 mg cm^{-2}) and catalyst layer thickness of 10 μm (20 μm) (Reum, 2008). The average density of the CCM before assembly was 1.6 g cm^{-3} , which was used for the dose calculations. The active area of the catalyst-coated membrane was reduced to 10 mm^2 (2.3 $\text{mm} \times 4.5 \text{ mm}$) by laser ablation of the catalyst layers by Laser-Micronics GmbH, similar as described by Schmitz *et al.* (2004). TGP-H060-based carbon-fiber paper (Toray) with a microporous layer (MPL) from Umicore (230 μm uncompressed thickness, 2.3 mm width, 13.4 mm length) was used as the gas diffusion layer in the case of the constant current density experiments. For the constant voltage measurement, a TGP-H060 GDL (180 μm uncompressed thickness) without an MPL was used instead.¹ Thin Teflon foils used as gaskets additionally defined the GDL compression as the spacer between the membrane and the flow fields. The flow fields were made from a carbon composite (BMA5, SGL Technologies) with an outer diameter of 3.5 mm . The flow field bearing used for compression of the cell (not shown in Fig. 1) consisted of two semi-shells of Vespel cylinders with an inner diameter of 3.5 mm and a wall thickness of 0.5 mm at the irradiation domain.

The irradiation experiments were performed at the TOMCAT beamline (Stampanoni *et al.*, 2006) of the SLS with the membrane electrode assembly (MEA) oriented perpendicular to the beam. Galvanostatic (CC) or potentiostatic (CV) cell operation and electrochemical impedance measurements were realised using a Bio-Logic SP-300 galvanostat/potentiostat. Three cells were operated at a temperature of 303 K with the hydrogen/oxygen feed humidified at room temperature (50% relative humidity) and one cell at 357 K with the hydrogen/oxygen feed humidified at a dew point of 355 K (90% relative humidity) for the galvanostatic irradiation experiments. These cells were operated at a constant current of 50 mA (0.5 A cm^{-2}) for at least 60 min before the first irradiation, with the cell voltage being stable for at least the last 30 min. Additionally, one cell was operated in potentiostatic mode at a cell temperature of 303 K with a 50% relative humidity hydrogen/oxygen gas feed. Here, the cell voltage was set to 600 mV 45 min before the irradiation. Cathode and anode stoichiometries were >10 for all cells. An overview of the cell control mode, temperature and beam intensities used is given in Table 1.

¹ The presence or absence of an MPL had no influence on the performance degradation in similar irradiation experiments at 303 K.

Table 1

Combinations of the cell operation mode, the cell temperature and beam intensities used during the irradiation experiments.

Operation mode	Cell temperature (K)	Beam intensity (%)
Galvanostatic	303	100
Galvanostatic	303	10
Galvanostatic	303	1
Potentiostatic	303	100
Galvanostatic	357	100

The 1 kHz and 10 kHz AC impedance of the cells was measured with a sample rate of 1 Hz and used as a measure of the ionomer (mainly the membrane) resistance. According to Makharia *et al.* (2005), the contribution of the catalyst layer ionomer resistance is larger for the 1 kHz impedance than for 10 kHz impedance. Because the complex 1 and 10 kHz impedances are in the 45° region of a Nyquist plot of the electrochemical impedance data, their real components are sufficient to discuss the relative changes in membrane and catalyst layer ionomer resistance.

The dimensions of the monochromatic beam with an energy of 13.5 keV were 5.6 mm height and 4.9 mm width, such that the catalyst layer was completely irradiated. The full photon flux density (6×10^{11} photons $\text{s}^{-1} \text{mm}^{-2}$) corresponds to a radiant power density of 130 mW cm^{-2} and is considered as 100% beam intensity. It was reduced by metal filter foils to 9.6% (20 μm copper and 20 μm iron) and 1.2% (50 μm copper). The filters were selected based on the data given by Henke *et al.* (1993) and the resulting beam intensity was verified by the analysis of X-ray radiography images without the cell in the beam. The beam intensity at the CCM was furthermore reduced by about one-third due to the absorption of the cell components other than the CCM (*i.e.* flow field, flow field bearing and gas diffusion layer). This was determined by the analysis of X-ray radiographies of the cell (MEA perpendicular to the beam) comparing catalyst-layer-containing and catalyst-layer-free cell areas. The CCM has an absorbance factor of about 0.125 (Roth *et al.*, 2012), which leads to an absorption of radiant power density of 10.9, 1.04 and 0.13 mW cm^{-2} in the CCM for 100, 9.6 and 1.2% beam intensity, respectively. The formulas used for the dose calculations are provided in Appendix A.

At 100% beam intensity, irradiation periods of 30 s were combined with 6.5 min beam-off periods to study the relaxation of the cell voltage between the irradiation periods. The irradiation periods of the reduced beam intensities of 10 and 1% were adjusted to 300 and 3000 s, respectively, such that the cells accumulated a comparable X-ray dose. The beam-off periods for the reduced beam intensities were kept constant for better comparability of the cell response.²

The product water of the galvanostatically operated cells was collected and analyzed for sulfate with a Metrohm 882 Compact IC ion chromatograph.

² Owing to a programming error, the beam-off periods after the fifth to the seventh irradiation period of the 10% beam intensity irradiation experiment were exceptionally reduced to 10 s.

3. Results

The development of cell voltage and the real part of the 1 and 10 kHz AC impedance during the irradiation experiments are shown in Fig. 2 for all cells operated at constant current density.

The cells at 303 K cell temperature lost 33 mV (100% beam) to 23 mV (1% beam) cell voltage during the first irradiation period. During the first beam-off period the cell voltages stabilized and recovered partially. The performance loss was similar (25 mV) for the cell irradiated by 100% beam intensity during the second irradiation period, but thereafter the cell voltage recovered only temporarily in the beam-off period and afterwards the cell voltage decreased continuously at a rate of -4.3 mV min^{-1} . During the third irradiation period the performance loss increased slightly to 33 mV and the cell voltage degradation rate stabilized at -16 mV min^{-1}

in the following beam-off period. During the fourth irradiation period the cell voltage increased temporarily by 11 mV but the cell voltage degradation rate increased thereafter to -83 mV min^{-1} . The cell voltage became negative at minute 109 of the experiment and the current was set manually to zero.

At 10% beam intensity, the cell lost about 16 mV in the second irradiation period and the loss of cell voltage flattened to -0.6 mV min^{-1} . A recovery of the cell voltage was observed no later than the second beam-off period, where the recovery of the cell voltage flattened to $+0.2 \text{ mV min}^{-1}$ before the third irradiation period. The degradation rate of the cell voltage increased to -8.3 and -9.9 mV min^{-1} within the third and fourth irradiation period, respectively, and finally up to $-17.8 \text{ mV min}^{-1}$ in the eighth and final irradiation period. The cell voltage became negative 4.1 minutes after the eighth irradiation period.

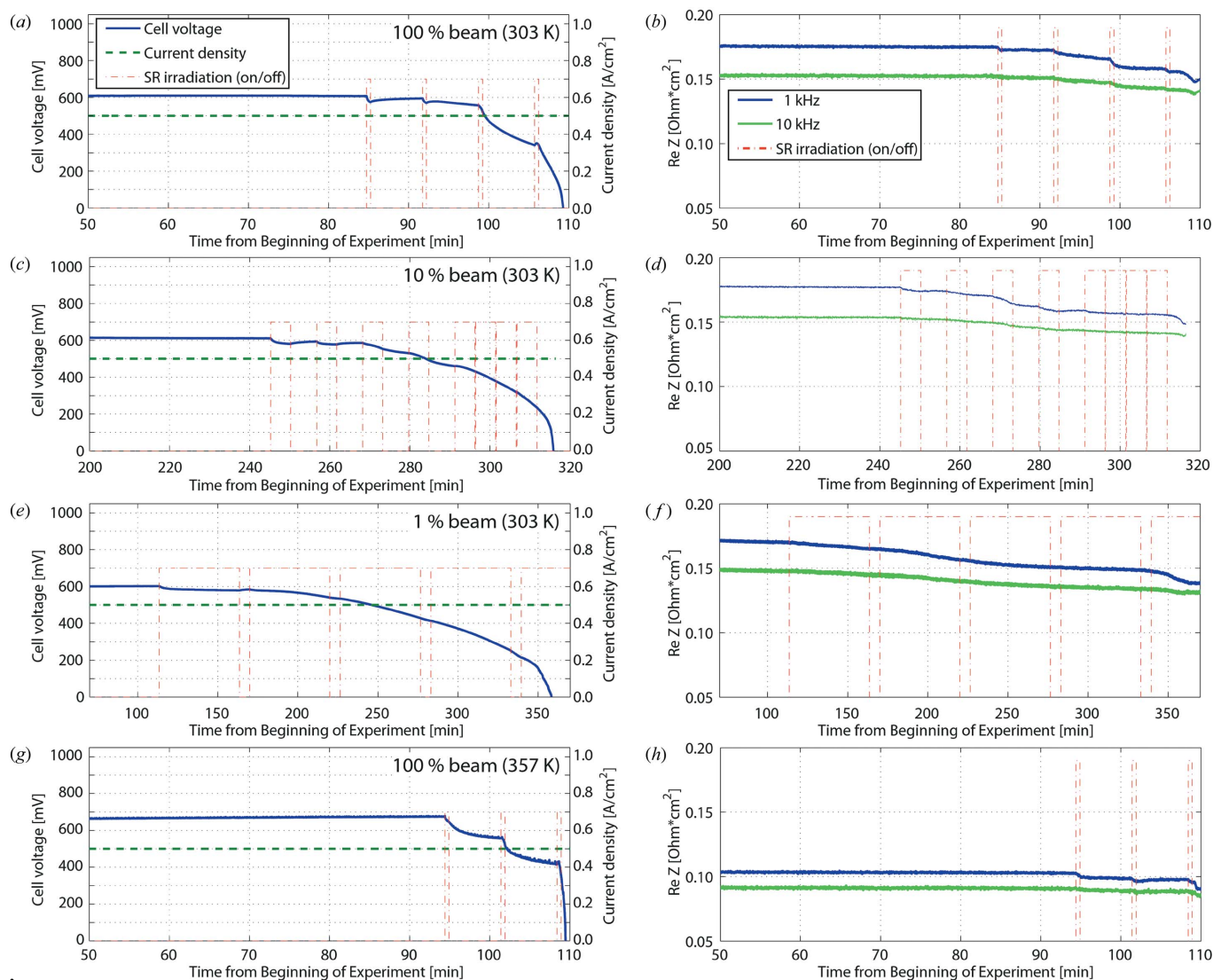


Figure 2 Time series data of cell voltage and current density (a, c, e, g), AC impedance (b, d, f, h) and X-ray shutter state (on/off) for the galvanostatic operation mode. Views (a) and (b) show 100% beam intensity at 303 K cell temperature, (c) and (d) 10% beam intensity at 303 K cell temperature, (e) and (f) 1% beam intensity at 303 K cell temperature, and (g) and (h) 100% beam intensity at 357 K cell temperature. Note the different time scales for the different beam intensities.

The cell irradiated at 1% beam intensity lost about 45 mV in the second irradiation period with a final cell voltage degradation rate of -1.8 mV min^{-1} , that lowered to -0.9 mV min^{-1} during the following beam-off period. The degradation rate of the cell voltage increased to -2.6 and -4.1 mV min^{-1} during the third and fourth irradiation period, respectively. Within the fifth irradiation period the cell voltage became negative and stabilized at about -130 mV (not shown).

The 357 K cell showed similar behavior during the first three irradiation periods with voltage losses of -31 to -68 mV . During the first and second beam-off periods no recovery of the cell voltage was observed, but the cell voltage degradation rate stabilized at values of -3.3 and -7.6 mV min^{-1} , respectively. After the third irradiation period, the cell voltage degraded fast, became negative and then stabilized at about -80 mV (not shown).

Interestingly, a recovery of the cell voltage was observed after the irradiation experiments. After operation in open circuit voltage for few minutes (typically a drying condition), the CC irradiated cells were able to provide 0.5 A cm^{-2} , at least temporarily, at positive potentials. A similar performance recovery has been reported in more detail by Eller *et al.* (2014).

The change in cell voltages as a function of the absorbed X-ray energy is summarized for cells operated at constant current density in Figs. 3(a) and 3(b). All cells show very comparable overvoltages up to an absorbed X-ray energy of about 0.33 J cm^{-2} (26 kGy). The degradation of the 303 K cells was furthermore very comparable up to an X-ray energy accumulation of about 1.0 J cm^{-2} (78 kGy), where the cells already showed a clearly biased cell voltage (80 to 120 mV additional overpotential). The steep decreases/increases of cell voltage at constant values of absorbed X-ray energy are due to ongoing degradation or recovery of the cell voltage during the beam-off periods.

The real part of the 1 and 10 kHz impedance decreased for all CC operated cells and beam intensities during the irradiation periods [see Figs. 2(b), 2(d), 2(f) and 2(h), as well as Figs. 3(c) and 3(d)]. In all cases, the 1 kHz impedance decreased more strongly than the 10 kHz impedance. It is therefore very likely that the catalyst layer ionomer, and consequently also the membrane, became better hydrated during the irradiation time due to reduced water contact angles (Roth *et al.*, 2012). The fact that all cells showed an obvious decrease of the 1 kHz impedance contemporaneous to the voltage reversal points furthermore towards flooding of the catalyst layer.

The development of the current density for the cell under potentiostatic control at 600 mV is shown in Fig. 4(a). The current density reduced from 0.56 A cm^{-2} to about 80% (0.45 A cm^{-2}) within the first irradiation period. In the following beam-off period it recovered to 0.51 A cm^{-2} . During the second irradiation period the current density dropped to 0.43 A cm^{-2} and recovered only slightly to 0.47 A cm^{-2} within the following beam-off period. After the third and fourth irradiation period, the current density did not recover and

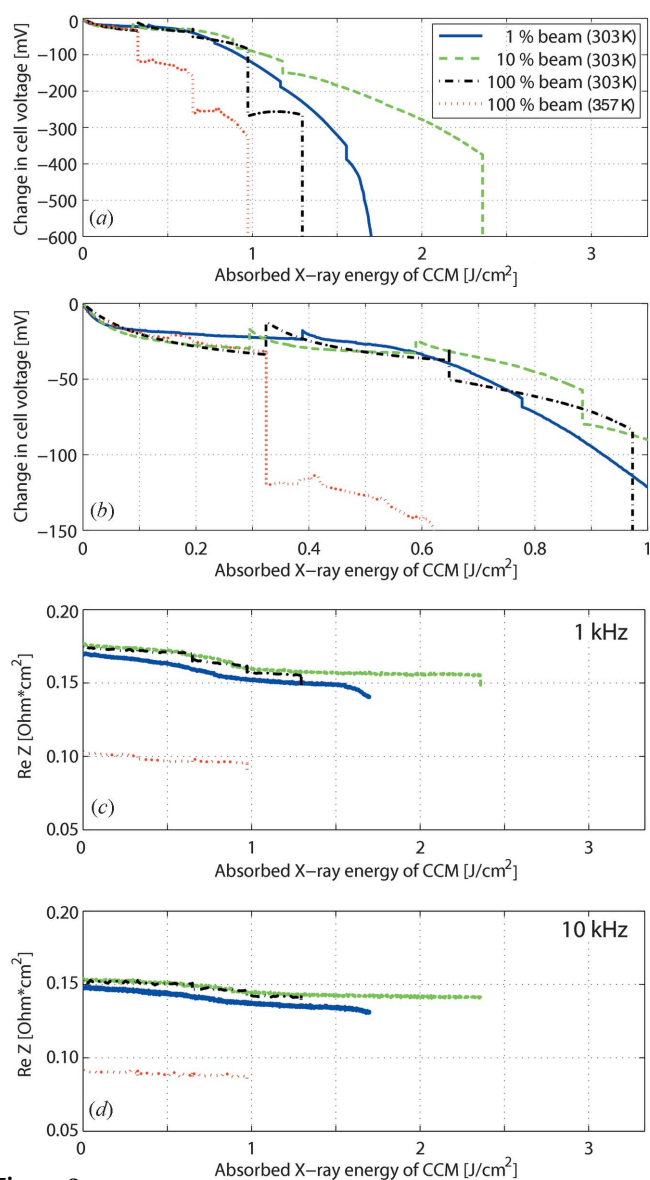


Figure 3

Change in cell voltage during galvanostatic operation as a function of the absorbed X-ray energy of the CCM ($1 \text{ J cm}^{-2} \equiv 78 \text{ kGy}$) in (a) overview and (b) details up to 1.0 J cm^{-2} ; with (c) corresponding real part of 1 kHz and (d) 10 kHz cell impedance; above 1.33 J cm^{-2} the beam-off time of the 10% beam cell was reduced to 10 s due to a programming error and beam-off voltage decay becomes invisible on that scaling.

dropped to below half (0.27 A cm^{-2}) and one third (0.18 A cm^{-2}) of its initial value, respectively. Even though the current density was decreasing during all later irradiation periods, it recovered to 0.20 A cm^{-2} within the fifth irradiation period. Also the later beam-off periods showed a minor recovery of the current density, but overall it reduced to 0.17 A cm^{-2} at the end of the tenth and final irradiation period. Twenty minutes after the last irradiation period the cell voltage was set to 100 mV. The current density raised shortly above 1 A cm^{-2} but then dropped within a minute to below 0.25 A cm^{-2} and seemingly converged towards 0.2 A cm^{-2} (not shown).

The AC impedance data of the potentiostatic operated cell is shown in Fig. 4(b). As the data was more noisy (5 mV

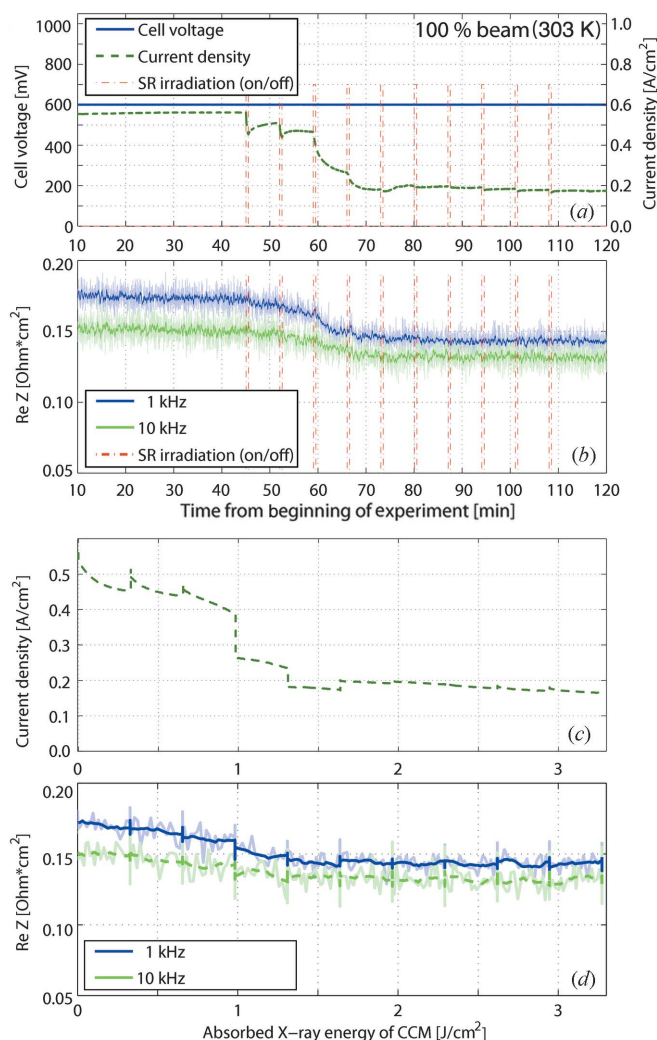


Figure 4 Time series data of cell voltage and current density (a), corresponding smoothed AC impedance (b) and X-ray shutter state (on/off) of the potentiostatic irradiation experiment; (c) current density as a function of the absorbed X-ray energy of the CCM ($1 \text{ J cm}^{-2} \equiv 78 \text{ kGy}$) and (d) corresponding smoothed AC impedance behavior. The raw AC impedance signal is given in lighter green and blue color for completeness.

perturbation amplitude) than for the galvanostatic operation (2 mA perturbation amplitude), a running mean average over ten data points is given as well. Reducing 1 and 10 kHz resistances were found up to the fifth irradiation, with the 1 kHz resistance lowering the stronger.

Figs. 4(c) and 4(d) show the development of the current density and AC impedance as a function of accumulated X-ray energy, respectively. The current density has already dropped by 10% after 0.08 J cm^{-2} . The prominent drop of the current density below 0.3 A cm^{-2} at 1.0 J cm^{-2} (78 kGy) shows again that the degradation processes continue, even when the beam is switched off. The slight increase of the 1 kHz impedance after 1.6 J cm^{-2} absorbed X-ray energy (125 kGy) suggests that drying of the electrode, due to the reduced current densities, leads to lower mass transport losses (c.f. Eller *et al.*, 2014) and a temporary recovery of the current density.

The analysis of the product water of the CC irradiated cells revealed a 5 to 38 times higher release rate of sulfate ions during and after the irradiation experiments of the cells. Variable sampling condition and duration do not allow for correlation between the sulfate release rates to the beam intensities, but a dose dependency can be expected (Paul *et al.*, 2013). Cathode catalyst poisoning by the sulfate species reversibly reduces the oxygen reduction reaction activity of the electrocatalyst (Kabasawa *et al.*, 2008) and was postulated by Schneider *et al.* (2010). It is therefore very likely as a second and reversible degradation effect in addition to the irreversible irradiation-induced changes of the wetting properties.

4. Conclusion

The degradation of cell performance under monochromatic X-ray exposure at 13.5 keV was studied in galvanostatic and potentiostatic operation modes at two different cell temperatures. The beam intensity was varied over a range of two orders of magnitude (6×10^9 to 6×10^{11} photons $\text{s}^{-1} \text{ mm}^{-2}$). The whole catalyst layer domain of PEFCs designed for X-ray tomographic microscopy was irradiated in a through-plane imaging direction (beam perpendicular to membrane).

At 303 K cell temperature and in galvanostatic operation mode the X-ray-induced cell performance degradation was found to be a function of X-ray dose and independent of beam intensity up to 1.0 J cm^{-2} of absorbed X-ray energy (78 kGy). Consequently, the degradation rate decreased with lower beam intensity. The scatter of the degradation at absorbed X-ray energies higher than 1.0 J cm^{-2} is no more relevant for unbiased imaging of water in PEFC, because X-ray-induced cell voltage bias exceeds about 100 mV and the resulting additional heat load to the cell might affect the liquid water distribution. Furthermore, the performance degradation was found to be more sensitive to X-ray irradiation at a higher cell temperature of 357 K and high-feed gas relative humidity of 90%. Under these conditions, already an accumulated X-ray energy of 0.33 J cm^{-2} (26 kGy) seems to be the critical limit.

These limits are only applicable if galvanostatic operation at constant current density can be guaranteed during the whole irradiation time for the irradiated cell domain. For X-ray imaging experiments using cells with active areas larger than the irradiated domain, equipotential conditions over the entire cell area must be expected both for the galvanostatic and the potentiostatic operation modes. Irradiation under potentiostatic control at 600 mV and a cell temperature of 303 K revealed a 10% decrease in current density already after an accumulated X-ray energy of 0.1 J cm^{-2} (8 kGy) and a 50% decrease after 1.0 J cm^{-2} (78 kGy), respectively. After 1.3 J cm^{-2} (100 kGy) of absorbed X-ray energy, the current density reduced to 32% decreasing only slightly with fluctuations to 30% after 3.3 J cm^{-2} (260 kGy).

Two different degradation mechanisms of X-ray-induced performance degradation were identified with partly irreversible and reversible contributions. According to the impedance data, the membrane and especially the catalyst layer

become better humidified with increasing X-ray dose. Shortly before the cell voltage reversal in galvanostatic operation mode, even indications for catalyst layer flooding were observed. This seems to be caused by irreversibly reduced water contact angles due to X-ray irradiation as reported by Roth *et al.* (2012) and would explain also the higher sensitivity to X-ray irradiation at high feed gas humidity.

The increased sulfate concentrations that were identified in the product water during and after X-ray irradiation suggest cathode catalyst poisoning by sulfate species from ionomer decomposition as a second but reversible source of degradation. The reduced degradation or even improvements of cell voltage during the early beam-off periods may result from different time scales of the catalyst poisoning by sulfate originating from catalyst layer ionomer or bulk membrane. The higher diffusivity of the sulfate species at increased cell temperature would also explain the faster degradation at 357 K cell temperature. The performance recovery that was observed after operation at negative cell voltages strengthens the sulfate poisoning hypothesis, as sulfate desorbs from the platinum surface at potentials below 0.3 V (Kabasawa *et al.*, 2008) and will be removed from the MEA with the product water.

Overall, these observations exclude ionomer dry-out due to beam absorption (Hartnig & Manke, 2012) as the major source of the performance loss for the investigated beam intensities.³

Finally it can be concluded that first of all, it is up to the experimentalist to decide on beam intensity and the corresponding time scale on which the acceptable dose is applied to the cell. Cells might be imaged for a few short periods at high beam intensities as needed for three-dimensional *in situ* XTM studies or exposed with low intensities over longer periods for two-dimensional radiography experiments. But if the cell area is larger than the irradiated area, the depicted water saturation might be biased (Eller *et al.*, 2014) already after accumulation of X-ray energies clearly below 1 J cm⁻² (78 kGy), since reduced local current densities have to be expected. Secondly, the through-plane irradiation set-up has to be considered as a worst case scenario for X-ray imaging. In-plane radiography or tomography configurations (beam parallel to membrane) should provide higher X-ray resistance due to the self-shielding of the MEA by the strong absorption of the beam in the boundary domains.

APPENDIX A

Calculation of absorbed X-ray energy and dose

The radiant power density \dot{P} [W cm⁻²] is given as

$$\dot{P} = \dot{\Phi} E_{\text{ph}} e \quad (1)$$

where $\dot{\Phi}$ is the monochromatic photon flux density [photons s⁻¹ cm⁻²] with a photon energy E_{ph} [eV photon⁻¹] and e is the

³ Compared with the electrochemical losses of the cell of about 300 mW cm⁻² already, the absorbed X-ray energy of the full beam intensity seems negligible for cell heat-up.

elementary electric charge. The absorbed radiant power density \dot{P}_{abs} of the CCM samples was calculated as

$$\dot{P}_{\text{abs}} = \dot{P} \alpha \quad (2)$$

where α is the absorption factor. The absorbed X-ray energy (density) \dot{E}_{abs} [J cm⁻²] of the CCM samples is then given as

$$\dot{E}_{\text{abs}} = \dot{P}_{\text{abs}} t \quad (3)$$

where t [s] is the duration of the irradiation.

Finally, the absorbed dose D [J kg⁻¹ = Gy] follows from

$$D = \frac{\dot{E}_{\text{abs}}}{10^{-3} \rho d} \quad (4)$$

where ρ [g cm⁻³] and d are the density and the thickness of the CCM sample, respectively.

Support at the beamline by S. Eberhardt, F. Marone and J. Roth, precise machining work by M. Hottiger, software and electronic support by T. Gloor and L. Băni, as well as discussions with P. Boillat about impedance analysis of catalyst ionomer conductivity and J. Roth about radiation damage are gratefully acknowledged.

References

- Alink, R., Hausmann, J., Markötter, H., Schwager, M., Manke, I. & Gerteisen, D. (2013). *J. Power Sources*, **233**, 358–368.
- Eller, J., Rosén, T., Marone, F., Stampanoni, M., Wokaun, A. & Büchi, F. N. (2011a). *J. Electrochem. Soc.* **158**, B963–B970.
- Eller, J., Roth, J., Marone, F., Stampanoni, M., Wokaun, A. & Büchi, F. N. (2011b). *ECS Trans.* **41**, 387–394.
- Eller, J., Roth, J., Marone, F., Stampanoni, M., Wokaun, A. & Büchi, F. N. (2014). *J. Power Sources*, **245**, 796–800.
- Görner, W., Hentschel, M., Müller, B., Riesemeier, H., Krumrey, M., Ulm, G., Diete, W., Klein, U. & Frahm, R. (2001). *Nucl. Instrum. Methods Phys. Res. A*, **467–468**, 703–706.
- Goto, S., Takeshita, K., Suzuki, Y., Ohashi, H., Asano, Y., Kimura, H., Matsushita, T., Yagi, N., Isshiki, M., Yamazaki, H., Yoneda, Y., Umetani, K. & Ishikawa, T. (2001). *Nucl. Instrum. Methods Phys. Res. A*, **467–468**, 682–685.
- Hartnig, C. & Manke, I. (2012). *Polymer Electrolyte Membrane and Direct Methanol Fuel Cell Technology*, Vol. 2, pp. 462–482. Cambridge: Woodhead.
- Hartnig, C., Manke, I., Kuhn, R., Kleinau, S., Goebbels, J. & Banhart, J. (2009). *J. Power Sources*, **188**, 468–474.
- Henke, B., Gullikson, E. & Davis, J. (1993). *At. Data Nucl. Data Tables*, **54**, 181–342.
- Kabasawa, A., Uchida, H. & Watanabe, M. (2008). *Electrochem. Solid State Lett.* **11**, B190–B192.
- Krüger, P., Markötter, H., Haussmann, J., Klages, M., Arlt, T., Banhart, J., Hartnig, C., Manke, I. & Scholta, J. (2011). *J. Power Sources*, **196**, 5250–5255.
- Lee, J., Hinebaugh, J. & Bazylak, A. (2013). *J. Power Sources*, **227**, 123–130.
- Makharia, R., Mathias, M. F. & Baker, D. R. (2005). *J. Electrochem. Soc.* **152**, A970–A977.
- Mukaide, T., Mogi, S., Yamamoto, J., Morita, A., Koji, S., Takada, K., Uesugi, K., Kajiwara, K. & Noma, T. (2008). *J. Synchrotron Rad.* **15**, 329–334.
- Paul, D. K., Giorgi, J. B. & Karan, K. (2013). *J. Electrochem. Soc.* **160**, F464–F469.

- Reum, M. (2008). PhD thesis, ETH Zurich, Switzerland.
- Roth, J., Eller, J. & Büchi, F. N. (2012). *J. Electrochem. Soc.* **159**, F449–F455.
- Schmitz, A., Wagner, S., Hahn, R., Weil, A., Schneiderlöchner, E., Trantz, M. & Hebling, C. (2004). *Fuel Cells*, **4**, 190–195.
- Schneider, A., Wieser, C., Roth, J. & Helfen, L. (2010). *J. Power Sources*, **195**, 6349–6355.
- Stampanoni, M., Groso, A., Isenegger, A., Mikuljan, G., Chen, Q., Bertrand, A., Henein, S., Betemps, R., Frommherz, U., Böhrer, P., Meister, D., Lange, M. & Abela, R. (2006). *Proc. SPIE*, **6318**, 63180M.
- Weitkamp, T., Tafforeau, P., Boller, E., Cloetens, P., Valade, J.-P., Bernard, P., Peyrin, F., Ludwig, W., Helfen, L. & Baruchel, J. (2010). *AIP Conf. Proc.* **1221**, 33–38.